

---

# STATIC IR DROP PREDICTION WITH ATTENTION U-NET AND SALIENCY-BASED EXPLAINABILITY

---

**Lizi Zhang**  
University of Wisconsin-Madison  
Madison, WI 53706  
lzhang697@wisc.edu

**Azadeh Davoodi**  
University of Wisconsin-Madison  
Madison, WI 53706  
adavoodi@wisc.edu

August 7, 2024

## ABSTRACT

There has been significant recent progress to reduce the computational effort of static IR drop analysis using neural networks, and modeling as an image-to-image translation task. A crucial issue is the lack of sufficient data from real industry designs to train these networks. Additionally, there is no methodology to explain a high-drop pixel in a predicted IR drop image to its specific root-causes.

In this work, we first propose a U-Net neural network model with *attention gates* which is specifically tailored to achieve fast and accurate image-based static IR drop prediction. Attention gates allow selective emphasis on relevant parts of the input data without supervision which is desired because of the often sparse nature of the IR drop map. We propose a two-phase training process which utilizes a mix of artificially-generated data and a limited number of points from real designs. The results are, on-average, 18% (53%) better in MAE and 14% (113%) in F1 score compared to the winner of the ICCAD 2023 contest (and U-Net only [1]) when tested on real designs. Second, we propose a fast method using *saliency maps* which can explain a predicted IR drop in terms of specific input pixels contributing the most to a drop. In our experiments, we show the number of high IR drop pixels can be reduced on-average by 18% by mimicking upsize of a tiny portion of PDN's resistive edges.

## 1 Introduction

Static IR drop analysis of power delivery network (PDN) is a crucial task to accelerate IC design closure in modern technology nodes. Today's PDN is a large-sized 3D resistive network spanning across many metal layers. Due to parasitics in the PDN, voltage drop is induced between the power pads and cells in the design. A common goal of the analysis is to identify the nodes of the PDN where the voltage drop is higher than an acceptable threshold which is typically referred to as the 'hotspots'. Fast IR drop analysis is crucial to identify and guide many rounds of optimizations often needed to remove the hotspots, and accelerate design closure.

Static IR drop analysis depends on: (1) topology of the PDN and resistance value of each branch in the network; (2) location of power pads on the PDN; (3) location and amount of current sources representing the cells or modules in the design. The underlying computation is based on solving a system of linear equations with millions to billions of variables [2, 3]. A commercial tool can take several hours to perform one round of analysis for modern designs.

Earlier work for PDN analysis trade off accuracy for speed by utilizing spatial locality [4], hierarchical methods [5], Krylov-subspace methods [6, 7], and multi-grid techniques [2]. More recently, machine learning (ML)-based techniques provide significantly faster and more accurate solutions [8, 9, 10]. But some are limited to incremental analysis and require retraining for each new design [8, 9]. The work [10] is based on Convolutional Neural Networks (CNNs) but assumes similar PDN resistance from each cell to power pads, and configuring sizes of tiles on the layout.

Most recently, [1] models the problem as an image-to-image translation task. Each of the three inputs is expressed as an image. A U-Net model which is a convolutional encoder-decoder NN is used to generate a predicted IR drop map. This model naturally handles 2D spatially distributed data without the need to set any tile size, and does not require a retraining for each design.

Despite the impressive success of ML-based approaches, an important, unresolved challenge is lack of sufficient data from real designs to train the NNs. Recently, [11] created a large training dataset for this purpose. It utilized adversarial models to artificially generate data which had realistic current maps. Open-source static IR drop solvers were then used to generate golden ground-truth. However, there has not been a systematic evaluation of how NNs trained with artificially-generated data perform on real designs. The ICCAD 2023 contest featured a problem on this issue [12].

Finally, an issue with [1] is lack of explainability of a predicted hotspot to its root-causes. As an example, consider that the output generated by [1] is an (2D) image but the PDN is a 3D structure. Predicting hotspots at specific pixels in a 2D image cannot be traced back to specific edges and layers. Neither can the hotspots be traced to other sources such as specific locations on an input current density map or specific power pads. The degree of contribution of each of these cannot be determined. This explainability is a highly desired next step to guide optimizations to reduce the hotspots.

**In this work**, to address the above issues, we first propose AttUNet, a neural network model based on U-Net embedded with *attention gates*. Attention gates allow selective emphasis on relevant parts of the input data without supervision. This allows the model to focus on useful information during the learning process. Use of attention gates is motivated by the often sparse nature of the IR drop maps. In addition, the U-Net architecture is designed for the task of single-image to single-image prediction. However, IR drop is a multi-image to single-image prediction task. To handle this issue, we also embed the U-Net architecture with a new preprocessing convolutional block which introduces an initial per-image filter.

Next, we leverage a *pretrain-finetune* strategy. We first train AttUNet using a large volume of artificially-generated data. A few data points from real design are then used in a final fine-tuning. We apply image transformation to augment the training data to improve the robustness of the training.

Finally, we propose a procedure to generate *saliency maps* [13] for a predicted IR drop map. These maps allow measuring degree of contribution of each pixel of each input image to any pixel in the output image. They are found via backward propagation of the output image and computing gradients with respect to each input pixel. A main advantage of saliency maps is the very low computational effort to generate them (e.g., seconds) without the need to modify the model. In contrast, existing techniques for explainability of NNs often require modifying the model, e.g., by adding a new layer which compromises the performance [14, 15, 16].

The summary of our contributions is listed below:

- We propose AttUNet, a new variation of UNet with embedded attention gates, tailored for the IR drop problem which is by nature a multi-image to single-image prediction task.
- We adapt a ‘pretrain-finetune’ transfer learning strategy which is able to avoid overfitting and thus handle the issue of lack of sufficient data from real designs. We apply a data augmentation step to improve the robustness of training.
- We propose a procedure to generate saliency maps for a predicted IR drop image which allows measuring the contribution of each input feature to predicted high-drop pixels.

In our simulations we use the ICCAD 2023 contest setup which provides a hundred of artificially-generated data points and few points of real designs. When measuring performance on real designs only, we show AttUNet is on-average 18% (53%) better in MAE and 14% (113%) in F1 score compared to the winner of the recent ICCAD 2023 contest (and U-Net only [1]). We also use saliency maps for predicted high-drop pixels to guide PDN optimization. We show the number of predicted high IR drop pixels can be reduced on-average by 18% by upsizing a tiny portion of resistive edges of the PDN.

## 2 Proposed Methodology

Figure 1 shows the overall flow of our approach. The inputs to the problem are (1) current map which has the distribution of current sources (representing modules/cells) in the design; (2) PDN density map which includes the topology of the PDN and resistance values of each connection (via/metal layer); (3) map of effective distance to power pads which has the locations of all voltage sources (power pads) in the design.

The AttUNet neural network receives these inputs and generates a predicted IR drop map as an image-to-image translation task. The first step shown in Figure 1(a) is to represent the inputs as images. We use 3 images representing the 3 inputs to the problem as in [1]. Additionally, we translate the spice file describing all the layers into multiple images corresponding to each individual layer. These are explained in Section 2.1. Next, the AttUNet model is trained using the two-step pretrain-finetune strategy which is shown in Figure 1(b). Before training, we first augment input images by applying image transformations to increase the training size which helps improve the robustness of the

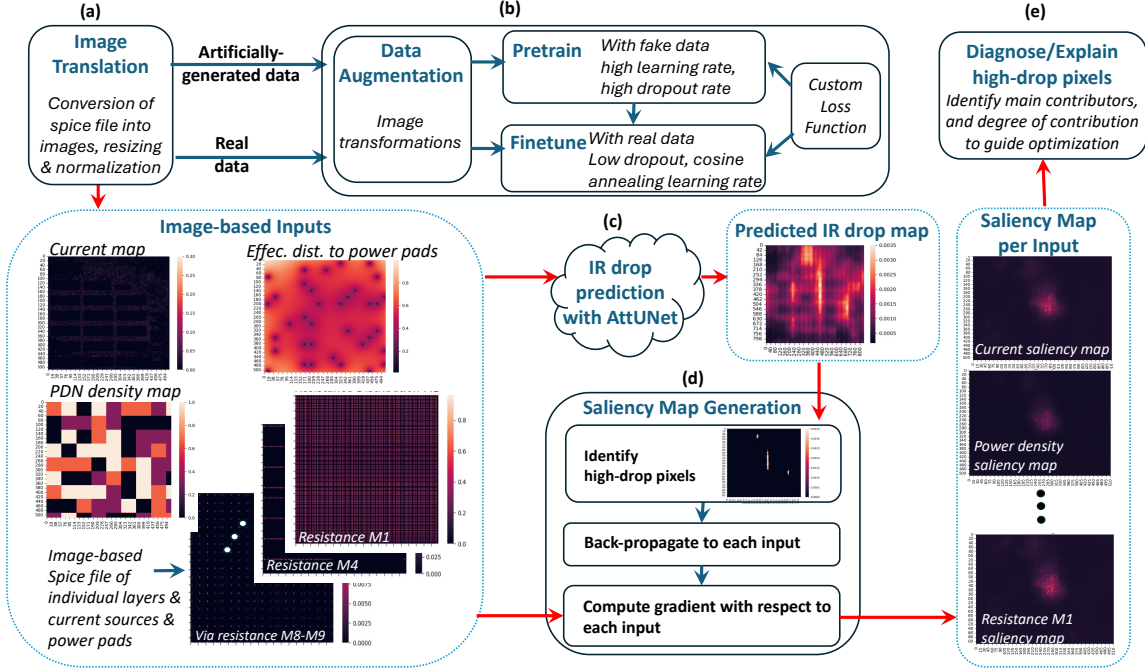


Figure 1: Components of our methodology: (a) image translation; (b) data augmentation and two-step training; (c) inference with attention U-Net; (d) saliency map generation; (e) explanation and diagnosis of predicted hotspots.

trained model. The details are explained in Section 2.3. Image-based inputs are then fed to the trained model for IR drop prediction as shown in Figure 1(b). We discuss the AttUNet model for IR drop prediction in Section 2.2.

After generating an IR drop map, saliency maps are generated as shown in Figure 1(d) and discussed in Section 2.4. Here, first high-drop pixels are identified from the generated IR drop map. The output of this step are individual saliency maps (one per input image). These saliency maps can be directly compared to each other because they are generated from normalized image-based inputs. They highlight degree of contribution of individual pixels of each input image to identified high-drop pixels which can be used to guide optimizations in order to generate a cooler IR drop map image.

## 2.1 Image-based Inputs

The first step prior to inference or training is to translate the inputs to image-based format. We explain how this is done including resizing and normalization operations relative to the setup in the recent ICCAD 2023 contest [12] which we used in our experiments. For each design, 3 image-based and 1 spice file describe the problem inputs. The 3 image-based inputs are described in detail in [1, 12].

They correspond to the current map, PDN density map, and effective distance to power pads. (Current map shows locations of current sources. PDN density map reflects the spacing between power stripes per unit area across all metal layers. Map of effective distance to power pads reflects the distance of each PDN node to all power pads, given by  $\sum_{i=1}^N d_i^{-1}$  where  $N$  is the number of pads and  $d_i$  is distance to the  $i^{th}$  pad.) These 3 inputs are expressed in matrix format where each entry in a respective matrix represents a pixel for an image-based representation. An entry in any of these matrices represents the value of the corresponding entity in the lowermost metal layer in  $1\mu m \times 1\mu m$  area of the chip.

*Converting Spice File into Additional Image-Based Inputs:* In addition to the above 3 image-based inputs, in this work, a spice file is added to describe detailed information across each individual metal and via layer. It contains locations of PDN node, value of resistances between the nodes, current source nodes and their values, and voltage source nodes. We extract multiple image-based files from this single spice file, where each new file correspond to the data of a specific metal or via layer. These are encoded in a similar matrix format. Each entry (pixel) represents a lumped resistance in a  $1\mu m \times 1\mu m$  area. Specifically, for the ICCAD 2023 contest setup, we extract image-based files corresponding to resistances of layers M1, M4, M7, M8, M9, and via layers M14, M47, M78, M89.

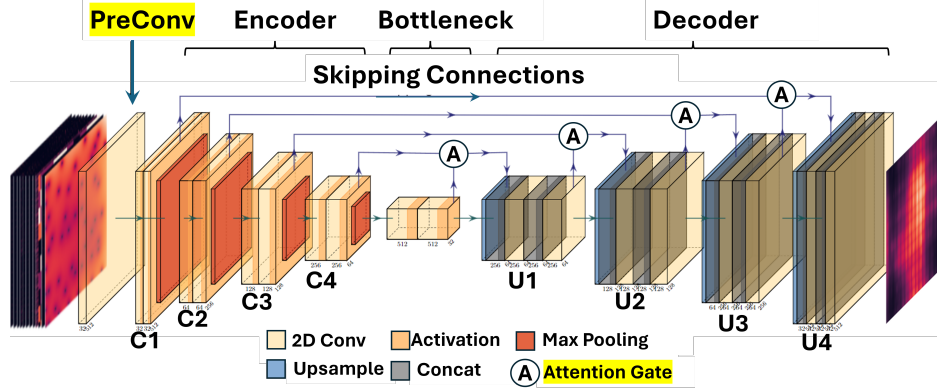


Figure 2: Block diagram of AttUNet. Additional embedded components compared to a U-Net structure are highlighted.

**Resizing and Normalization:** Since the chip dimensions may be different, next we apply resizing to adjust all image-based inputs to the same dimension to allow processing by the same NN model. In general chip dimensions may vary among testcases. For example, in the ICCAD 2023 contest, they range from  $80 \times 80$  to  $1000 \times 1000$ . In our implementation, and for this range, we resized all inputs to  $512 \times 512$  to feed the neural network. (This is in part because the encoder in the AttUNet model downsizes the images by power of 2 at each level.) For dimensions below  $512 \times 512$  upsizing is applied. It is done in a similar way using interpolation to fill in the ‘new pixels’. Anti-aliasing is enabled while resizing images to alleviate distortions. Typically, the distortions resulting from this resizing process are minor and have minimal impact on the performance of the model<sup>1</sup>. Finally, for better adaptability, each input image is scaled to  $[0, 1]$  by dividing by its maximum matrix entry.

## 2.2 U-Net Shaped Network with Attention Gate

We give a brief overview of the U-Net architecture which was also used in [1] for IR drop prediction. We discuss its limitations to motivate for our new embedded blocks. Figure 2 shows structure of AttUNet. Added blocks compared to U-Net are highlighted.

U-Net structure is well known for its great performance in image segmentation tasks. It has the ability to extract and exploit features to generate an image-based output. A U-Net consists of 4 major parts: encoder, bottleneck, decoder and skipping connection. Encoder, also called downsampling path, utilizes a sequence of double-convolutional blocks, each followed by batch normalization, a rectified linear unit (ReLU) and a max pooling layer. The bottleneck connects the encoder to the decoder. It is a double-convolutional block that receives feature maps which have a high number of channels (i.e., 512 in our implementation).

The decoder is also composed of double-convolutional blocks, but instead of having a max pooling layer at the end, it has an upsampling layer at its beginning. A skipping connection exists between each encoder and decoder to pass global information of inputs to layers that are closer to outputs. Skipping connections allow the model to have a high-level view of the features and corresponding location information. The final layer is a  $1 \times 1$  convolution that is used to map features to the desired number of classes.

There are several limitations of the U-Net model that make it less effective when dealing with IR-drop prediction. Firstly, it is originally designed for problems with single-image input. (The input is one image with multiple channels.) In double-convolutional blocks, all channels are added together to generate new feature maps, which is effective for single-image problem because these channels have great similarity among each other and share the same features such as corners, edges, etc. However, for IR-drop prediction, the inputs to the model are multiple images and the images are very different from each other. Addition across channels entangles different features together and extracts inappropriate features by the model which can degrade the prediction performance.

Moreover, U-Nets works best for image labeling and image segmentation, where the outputs are relatively simple (e.g., a single value). In contrast, in IR-drop prediction, a value should be predicted for each pixel in the output image and for the full-chip scale which is normally more than 10,000 pixels.

<sup>1</sup>We note, before conducting any evaluations in our experiments, we first resize each predicted IR drop map back to its original dimension to compare with a ground-truth.

To overcome these limitations, we propose AttUNet which is a new U-Net shaped neural network with new embedded components so it is better tailored for the multi-image-to-single-image translation tasks such as IR-drop prediction. The new components are highlighted in Figure 2. We discuss each below.

*PreConv Block:* The AttUNet network has an additional PreConv block inserted as the first layer to preprocess the inputs. The PreConv is a convolutional layer which modifies the inputs channel-wise before passing them to the encoder. It has a single convolution block with  $2 \times 2$  filter and an activation function ReLU for each image-based input. The PreConv block works as a quick filter to highlight the salient features of each image-based input. Moreover, the convolution kernels (filters) scale each channel by assigning distinct weights to them, which reflect the overall significance of each channel. This preprocessing layer allows further convolution operations in U-Net to work with more relevant and distinguishing features, and better handle IR drop prediction as a multi-image to single-image task.

*Attention Gates:* These gates are added to the skipping connections between each pair of encoder and decoder in Figure 2. They function as auxiliary components that selectively emphasize or suppress specific regions of the input data without supervision, enabling the model to concentrate on pertinent information throughout the learning phase [17]. Given that the image-based inputs to IR drop problem are often sparse matrices (e.g., large portion of current maps are nearly zero), such regions have minimal contribution to IR-drop and can be suppressed by attention gates.

Our work uses the vector concatenation-based attention gate proposed in [17, 18] as shown in Figure 3. The two inputs are feature maps coming from a lower-level encoder, and a gate signal (which are feature maps coming from either bottleneck or decoder).

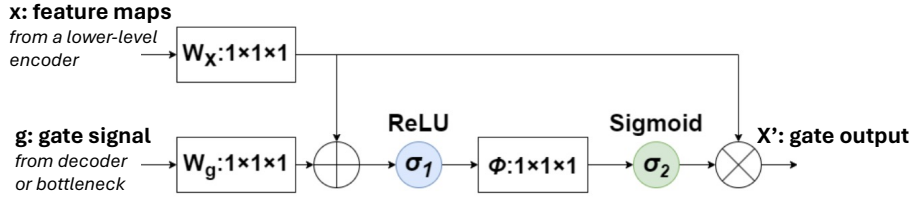


Figure 3: Vector concatenation-based attention gate.

Denote  $x_i \in \mathbb{R}^{C_x}$  and  $g_i \in \mathbb{R}^{C_g}$  to be the vector elements of input feature maps and gate signal, respectively. The attention gate function can then be expressed as follows:

$$\alpha_i = \sigma_2(\phi^\top(\sigma_1(W_x^\top x_i + W_g^\top g_i + b_g)) + b_\phi) \quad (1)$$

$$x'_i = x_i \cdot \alpha_i \quad (2)$$

The linear transformations are  $W_x \in \mathbb{R}^{C_x \times C_l}$ ,  $W_g \in \mathbb{R}^{C_g \times C_l}$ ,  $\phi \in \mathbb{R}^{C_l \times 1}$  and the bias terms are  $b_g \in \mathbb{R}^{C_l}$ ,  $b_\phi \in \mathbb{R}$ , and  $\sigma_1$  is ReLU activation and  $\sigma_2$  is the sigmoid activation function.

The output is element-wise multiplication of  $x_i$  and  $\alpha_i$ . Computation of  $\alpha_i$  in (1) can be further expressed as:

$$\alpha_i = \sigma_2(\phi^\top(\sigma_1(W^\top [x_i, g_i] + b)) + b_\phi) \quad (3)$$

where  $W \in \mathbb{R}^{(C_x+C_g) \times C_l}$  is concatenation of  $W_x$  and  $W_g$  along the second dimension.  $[x_i, g_i]$  is a vector concatenation of  $x_i$  and  $g_i$ . This operation is also the reason why this attention gate is called vector concatenation-based attention gate.

With expression in (3), the linear transformation can be easily done by using convolutions directly on gate inputs with  $1 \times 1$  kernel and  $C_l$  output channels. Then, the processed feature map is activated by a ReLU function and is linearly mapped to a  $\mathbb{R}^{C_l}$  space. The output of sigmoid activation function  $\alpha \in (0, 1)$  is known as attention map (or coefficients). These coefficients assign weights to each value of input feature maps coming from the encoder. The attention gate also receives the gate signals from deeper layers (e.g., bottleneck or decoder) to suppress irrelevant information and noise as they go through a skipping connection.

### 2.3 Data Augmentation and Model Training

We use a ‘pretrain-finetune’ strategy for training AttUNet as shown in Figure 1(b). First, pretrain is done using large volume of artificially-generated data. Next, finetune is done using limited data from real designs. (The provided dataset in the ICCAD 2023 contest contains 120 test cases in total, of which 100 are artificially-generated explained in [11, 12], and the remaining 20 are real. ) Each test case is represented as image-based inputs as discussed in Section 2.1, and is also accompanied by an image-based golden output voltage file.

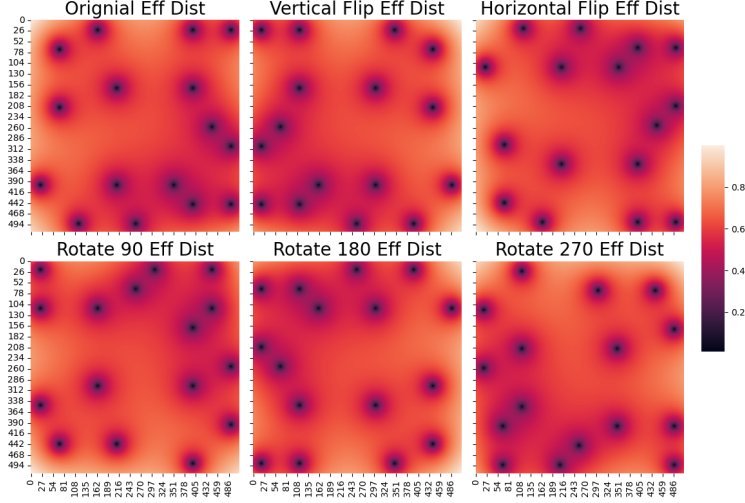


Figure 4: Augmenting the training data via five transformations applied to each image-based input.

*Data Augmentation:* As shown in Figure 1(b), we first augment the training data by applying multiple transformations to each image-based input which help improve the robustness of the model [19] especially when training data is not sufficient. Specifically, we apply the following five operations to each image-based input: vertical and horizontal flipping and three (counter-clockwise) rotations as shown in Figure 4 for a sample effective distance map. Next, a new testcase is generated by applying one of the five operations to an existing testcase; For instance, vertically flipping all the image-based representations within a testcase generates a new augmented testcase. This process results in a sixfold increase in the number of testcases, and enhances the diversity and robustness of the dataset [19]. It is applied to both artificially-generate data in pretrain phase, as well as real data in finetune phase.

We note, horizontal and vertical flippings only rearrange the elements in matrix representation of each input. These do not alter the validity of the results when solving the linear system of equations describing the IR-drop problem. Similarly, rotation operations essentially prompt the network to view the images from different angles, ensuring the results remain valid. The rotation angles are restricted to  $90^\circ$ ,  $180^\circ$ ,  $270^\circ$  to avoid cropping and centering operations which may change the resulting IR-drop.

*Model Training:* To train AttUNet, a transfer learning approach is employed. First, the pretraining phase aims to maximize the utilization of generative fake data. (The fake data contains meaningful input-output information because according to [11], an actual open-source IR drop solver is used to generate its golden ground-truth.) Next, finetuning is conducted only based on real data.

The learning rate and drop rate of the pretrain and finetune phases are listed in Table 1. For the pretraining phase, we first use a relatively high learning rate of 0.0005 and a high dropout rate from 0.3 to 0.5. For the fine-tuning phase which is based on real data, we adjust to a finer learning granularity, ranging from 0.0005 to 0.00001. Also, a cosine annealing learning rate with restart is applied in the finetune phase which can be expressed as follows:

$$\eta_t = \eta_{min} + \frac{1}{2}(\eta_{max} - \eta_{min})(1 + \cos \frac{T_{cur}}{T_{max}} \pi) \quad (4)$$

where  $\eta_{max}$  is set to be the initial learning rate 0.0005,  $\eta_{min}$  is the lowest learning rate 0.00001. The parameter  $T_{cur}$  is the number of current epochs and  $T_{max}$  is the number of total training epochs (600). As shown in Figure 5, learning rate oscillates with a decreasing frequency with increase in epochs. This provides a balance between rapid exploration of the parameter space at higher learning rates and finer optimization in regions of interest at lower learning rates.

Cosine annealing helps the model converge faster during the early stages of training [20]: By starting with a higher learning rate and gradually reducing it, the optimization process becomes more efficient. The cyclical nature of learning rate also allows the model to escape local minima to better explore the loss landscape.

As a final consideration during training, we employ a custom loss function. We note, the goal of IR-drop analysis is to predict the hotspot locations. Underestimating these is undesirable. Therefore, we define a custom loss function while training the model, which motivates the model to err on the side of overestimating the IR-drop, even if it results in a larger error. The loss function is set to punish more when a predicted value is less than the actual value. which can be



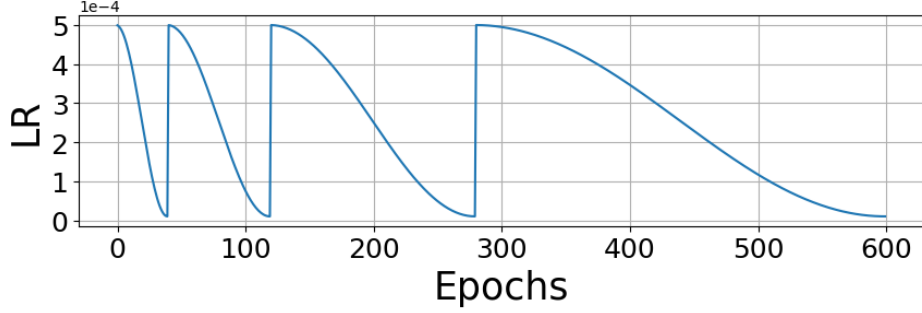


Figure 5: Illustration of the cosine annealing learning rate.

expressed as

$$Loss = \begin{cases} \frac{1}{n} \sum_{i=1}^n \|x_i - y_i\|, & \text{if } x_i \geq y_i \\ \frac{\lambda}{n} \sum_{i=1}^n \|x_i - y_i\|, & \text{if } x_i < y_i \end{cases}$$

where  $\lambda \geq 1$  is a constant,  $n$  is the number of pixels in the output figure,  $x_i$  is the predicted value and  $y_i$  is the ground truth. We set  $\lambda = 2$  in our experiments.

## 2.4 Fast Explainability with Saliency Maps

A predicted IR-drop map can be used to identify high-drop areas (which are individual pixels in the generated image-based output). A desired next step is to understand which specific inputs to the neural network are most responsible for these high-drop areas. This would be identifying specific image-based inputs, and specific pixels within each image since our problem is a multi-image to single-image prediction task. Among these identified input pixels, we would also be able to compare how much is the contribution of each one to the predicted high-drop pixels at the output.

These diagnosis help guide necessary optimizations to create a ‘cooler’ IR-drop map. For example, if specific pixels in the current map are found to have the highest contribution then it suggests that changing the floorplan of modules or placement of cells may be most appropriate to reduce the current demand at those locations. If the highest contributors are specific PDN edges on specific metal layers, then slight upsizing of these edges may be most appropriate. Such explainability has not been explored in any prior work for static IR-drop prediction and is a natural and important next step.

However, AttUNet, like most deep neural networks, operates more as a ‘black box’ which makes it difficult to comprehend the reasoning behind having specific output predictions. Existing techniques for adding explainability to a deep neural network often require changing the network structure, for example by adding extra layer(s) which can in turn compromise the performance [14, 15, 16]. However, saliency maps are available tools which allow gaining some insights into model behavior very quickly (e.g., seconds in our problem). In particular, for our problem which is an image-to-image translation task, we show the insight gained by saliency maps can be helpful for diagnosing the predicted high-drop pixels.

Figure 1(d) shows the process of generating the saliency maps. The first step is identifying high-drop pixels from the predicted IR-drop map. This relies on the designer to know how much IR-drop is considered acceptable given the desired specifications. Next, a back-propagation is done from this *high-drop-only* output map to each individual pixel on the input side. Finally, a gradient is computed with respect to each input. Since all image-based inputs are normalized to [0,1] range, the corresponding gradients are comparable across the pixels of different inputs. In the end a saliency map is generated for each image-based input, as shown in Figure 1(d).

Formally, let  $F_k : \mathbb{R}^{C \times h \times w} \rightarrow \mathbb{R}$  denote the function describing how the model generates the  $k^{th}$  pixel in the output image from the  $C$  (single-channel) input images. Each image (inputs or the output) has a height  $h$  and width  $w$  in AttUNet. Let  $F_k(X) = y_k$ ,  $X \in \mathbb{R}^{C \times h \times w}$  denote all input images as a 3D matrix representing a collection of individual single-channel 2D inputs. Also  $y_k \in \mathbb{R}$  is a pixel  $k$  of the generated output image.

Due to the complex nature of the neural network,  $F_k$  is a highly non-linear function of  $X$ . However, given an input  $X_0$ ,  $F_k(X_0)$  can be approximated with a linear function in the neighborhood of  $X_0$  by computing the first-order Taylor expansion [13]:

$$F_k(X) \approx w^T X + b$$

Table 1: Model hyperparameters and training parameters

Model hyperparameters	PreConv	filter size # filters	2×2 12
	C1	filter size # filters	3×3 32
	U1	filter size # filters	3×3 64
	C2	filter size # filters	3×3 128
	U2	filter size # filters	3×3 256
	C3	filter size # filters	3×3 512
	U3	filter size # filters	3×3 512
	Bottleneck	filter size # filters	3×3 512
Training parameters		Pre-train	Fine-tune
	Epochs	450	600
	Optimizer	ADAM	ADAM
	Learning rate	0.0005	0.00001-0.0005
	Dropout	0.3-0.5	0.1

where  $w$  is the derivative of  $F_k$  with respect to the input  $X$  at  $X_0$ :

$$w = \left. \frac{\partial F_k(X)}{\partial X} \right|_{X_0}$$

The magnitude of elements of  $w$  defines the importance of the corresponding pixels of  $X$  for the  $k^{th}$  pixel in output image.

The saliency map  $S \in \mathbb{R}^{C \times h \times w}$  is computed in the similar way. For a subset of output pixels  $\{y_k\}$ ,  $k = 1, 2, \dots, K$  (for example representing the predicted high-drop pixels), a (combined) saliency map  $S$  is generated for input  $X$  representing all image-based inputs. This is done by computing the average gradient regarding the subset of output pixels:

$$S = \frac{1}{K} \sum_{k=1}^K \frac{\partial F_k}{\partial X}$$

The above will have dimension  $C \times h \times w$  and further be broken into individual saliency maps representing each input-based image.

### 3 Experimental Results

The AttUNet model is implemented using Python 3.9 and under Pytorch 2.0.1 framework and is trained on two NVIDIA GeForce RTX 2080Ti GPUs. Table 1 describes the model hyperparameters and training parameters. Layer IDs are shown in Figure 2.

We used the data provided by the ICCAD 2023 contest [12]. As mentioned earlier, 120 test cases were provided, 20 of which corresponded to real designs and the rest were artificially-generated based on [11]. All 100 artificial data were used in the pre-train phase. From the 20 real designs, 10 were used in the fine-tune phase. The remaining 10 designs were used to test the model. To be comparable to the contest results, we use the same train/test split as the contest, that is using the same ten real chip data as testing dataset, and the remaining data for training.

As explained earlier, we pretrain AttUNet on augmented fake data and fine-tune on augmented real data. The augmentation enlarges the dataset by 6 folds, resulting in 800 pretrain data points and 80 fine-tune data points. The pretraining run time is 17.4 hours and fine-tuning is 4.6 hours. It is important to note that this is a one-time cost; the trained model can be applied directly to different chip designs and does not need any modifications. The average inference time across the designs in the testing dataset is 5.37 seconds.

We compare AttUNet with the UNet model in [1] which is named as IREDGe. We implemented this model based on the hyperparameters in [1]. For a fair comparison using the contest setup, we trained IREDGe using the same pretrain and fine-tune stages and same training data. For IREDGe, we used all training parameters reported in [1] except the



Table 2: Comparison of IR-drop prediction quality using the ICCAD 2023 contest setup. The unit for MAE is mV. Lower MAE and higher F1 score are desired.

	IREdGe [1]		ConvNeXtV2 (Contest Winner)		AttUNet	
	MAE	F1	MAE	F1	MAE	F1
Testcase7	0.124	0.648	0.066	<b>0.783</b>	<b>0.065</b>	0.469
Testcase8	0.110	0.698	0.082	<b>0.816</b>	<b>0.081</b>	0.428
Testcase9	0.205	0.120	<b>0.041</b>	<b>0.589</b>	0.067	0.169
Testcase10	0.141	0.483	<b>0.066</b>	0.532	0.090	<b>0.536</b>
Testcase13	0.119	0.417	0.207	0.000	<b>0.188</b>	<b>0.895</b>
Testcase14	0.192	0.034	0.422	0.000	<b>0.078</b>	<b>0.881</b>
Testcase15	0.157	0.000	<b>0.097</b>	0.088	0.115	<b>0.700</b>
Testcase16	1.066	0.000	<b>0.160</b>	0.529	0.338	<b>0.634</b>
Testcase19	0.131	0.037	0.091	<b>0.501</b>	<b>0.082</b>	0.330
Testcase20	0.089	0.000	0.118	<b>0.711</b>	<b>0.068</b>	0.156
Average	0.233	0.244	0.135	0.455	<b>0.110</b>	<b>0.520</b>

number of epochs and learning rate. These two were set the same as AttUNet which generated better results. We also added the same dropout as AttUNet.

Additionally, we compare with the winner of the ICCAD 2023 contest by directly using the quality metrics reported by the contest for the winning team. According to the contest website, the winning team uses a modified version of the ConvNetXTV2.

To measure quality of prediction, we use the same metrics given in the contest. These are (1) Mean Absolute Error (MAE) and (2) F1 score. First, MAE is computed as the absolute error between predicted IR-drop and the ground-truth given by:

$$MAE = \frac{\sum_i^N |\hat{V}_i - V_i|}{N}$$

where  $\hat{V}$  is predicted IR drop,  $V$  is ground truth and  $N$  is number of pixels. This metric reflects an *overall* prediction accuracy.

To compute an F1 score, first the highest 10% IR drops are labeled as positive and the rest as negative. The F1 score is given by:

$$F1 = \frac{2 \times precision \cdot recall}{precision + recall}$$

$$Recall = \frac{\text{True Positives}}{\text{True Positives} + \text{False Negatives}}$$

$$Precision = \frac{\text{True Positives}}{\text{True Positives} + \text{False Positives}}$$

where precision is the ratio of true positive predictions to the total number of predicted positives, and recall is the ratio of true positive predictions to the total number of actual positives. F1 score assesses the trade-off between precision and recall.

### 3.1 Prediction Quality

Table 2 compares our F1 score and MAE to [1] and the contest winner. The bold entries indicate the best MAE and F1 score in each row. First, AttUNet significantly outperforms IREdGe (on-average 113.3% in F1 score and 52.7% in MAE) under the contest setup. Furthermore, AttUNet outperforms ConvNeXtV2 in many cases. It is better in 9 out of 10 designs in at least one metric (MAE or F1 score). It achieves the lowest average MAE (0.110 mV) and highest average F1 score (0.520) among all test cases which is about 18.1% improvement in MAE and 14.3% in F1 score compared to ConvNeXtV2. Notable improvements are in test cases 13 and 14, in which ConvNeXtV2 has a 0.000 F1 score, indicating an inability to highlight the severe IR drop regions. AttUNet has F1 scores of 0.895 and 0.881 for these.

Figure 6 shows the output of AttUNet in testcase 9. As shown in (a) and (b), our prediction closely aligns with the ground truth in spotting the high-drop areas. Figures (c) and (d) show the map and distribution of MAE. Location of the

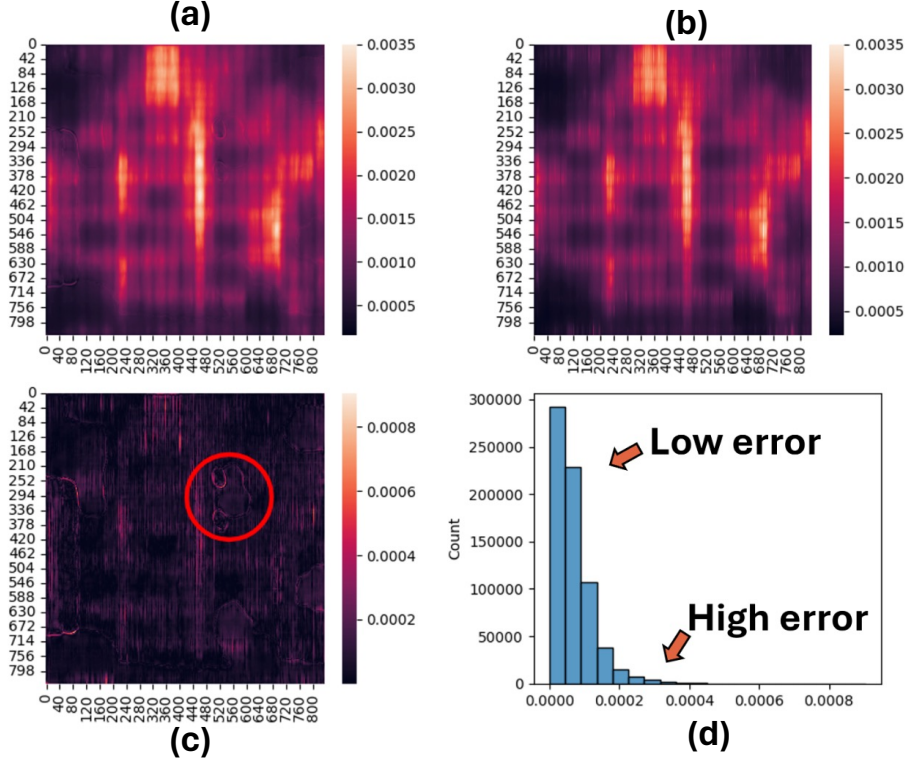


Figure 6: Results for testcase 9: (a) ground truth map, (b) map generated by AttUNet, (c) MAE map (d) Distribution of MAE.

Table 3: Comparison of the two metrics (averaged) shown for the training set (and the testing set, in parenthesis).

	Pre-trained Model		Fine-tuned Model	
	MAE (mV)	F1 Score	MAE (mV)	F1 Score
IREDDge	0.23 (1.14)	0.24 (0.17)	0.13 (0.23)	0.32 (0.24)
AttUNet	0.07 (0.38)	0.57 (0.32)	0.05 (0.11)	0.54 (0.52)

spots with higher prediction error can be seen in (c) such as the circled region. However, from the distribution we can see that most-frequent error bin (left-most bar in (d)) is about 0.2 mV. This value is significantly smaller than of the high error bins (which are higher than 3.0 mV).

### 3.2 Training Efficiency

Table 3 shows the average training (testing) MAE and F1 scores of IREDGe, AttUNet at different training stages. After fine-tuning, AttUNet achieves an MAE of 0.0520 mV and F1 score of 0.541. The MAE is significantly smaller compared to IR-drop values which normally range from 1–10 mV. Compared to IREDGe, AttUNet has better training and testing performances in terms of both average MAE and F1 score, indicating the effectiveness of learning and fitting the patterns and relationships present in the training data.

Given the inadequacy of real data, pre-training with generative fake data serves as a preventive measure against the potential risk of over-fitting. Generative errors (gaps between training MAE and testing MAE) decreases from 0.31 to 0.06 after fine-tuning, showing a great reduction in over-fitting risks. Also, F1 score after fine-tuning is at the same level in training and testing datasets. In comparison, IREDGe shows much bigger generative errors, which are 0.91 after pre-training and 0.10 after fine-tuning, indicating a significant possibility of over-fitting.

Figure 7 shows the output of AttUNet in the early stage of fine-tuning, specifically after 50 epochs. When the model is pre-trained (middle figure), the output shows clear boundaries that successfully separate regions with high IR-drop. In contrast, the model without pre-training (shown in right) lacks these distinctive features.

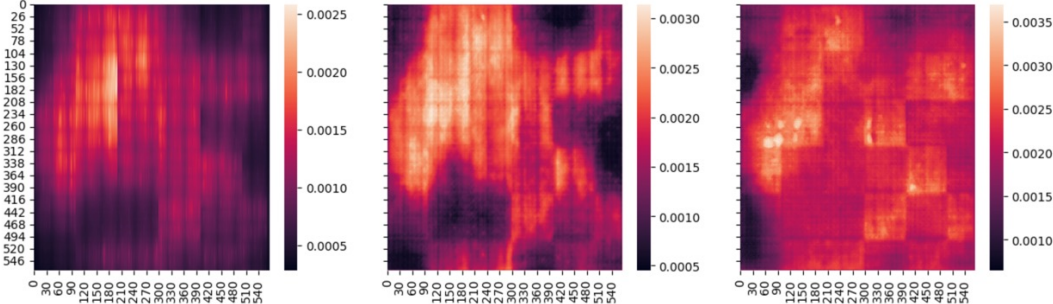


Figure 7: Impact of pre-training: Ground truth (left); AtUNet after pretraining and 50 epochs of fine-tuning (middle); same AtUNet but without pretraining (left).

### 3.3 Explainability with Saliency Maps

In this experiment, we first generate a saliency map for each image-based input. Recall, this requires identifying high-drop pixels from the predicted IR-drop image at the output. Specifically, for each testcase, we identify the maximum predicted voltage drop across all pixels which we denote by  $Dr_{max}$ . We then extract *high-drop* output pixels as those with a drop higher than  $Dr_{th} = 0.9 \times Dr_{max}$ .

Once saliency maps are obtained, we identify the top  $K$  pixels from the input images which have the highest contribution to these high-drop output pixels. To identify the top  $K$  input pixels, we first compute an average saliency for each input image by averaging the top  $K$  pixels. The input image with the highest contribution is the one with highest average saliency. Next, within that image we identify the top  $K$  pixels which have the highest saliency values.

Next we show how these top  $K$  input pixels can guide optimization to generate a new IR drop map with fewer high-drop pixels. The optimization that we considered in this experiment is upsizing the PDN wire branches corresponding to the top  $K$  input pixels. Therefore, we only considered the saliency maps of 5 metal layers (M1, M4, M7, M8, M9) and 4 via layers (M14, M47, M7M, M89). Other optimizations such as change in floorplan was not possible due to lack of more detailed layout information. Also, our emphasis in this experiment is to only show the impact of saliency maps. Exploring the best optimization is outside the scope of this work.

Table 4 shows the results for  $K = 100, 300, 500$ . We note these values of  $K$  represent a tiny portion of each  $512 \times 512$  input image. Our optimization mimics upsizing some PDN wire widths (thus reducing their resistances) which correspond to the top  $K$  pixels. Upsizing is mimiced by reducing the corresponding pixel values (in the corresponding image) by 10%. For example, in testcase 7 the top contributor layer is M1. It has 1574 high-drop pixels in the predicted output image. We identify only  $K$  pixels in the image input corresponding to M1 for optimization.

Next, we feed this slightly-optimized input back to AtUNet to predict a new IR-drop map. Using the same  $Dr_{th}$  as earlier, we then identify the number of high-drop pixels in the optimized map. We report percentage reduction in the number of high-drop pixels in Table 4. On-average the number of predicted high-drop pixels are reduced by 18.48%, 37.28%, 49.05% for  $k = 100, 300, 500$ , respectively.

To show identifying these top  $K$  pixels for optimization is not trivial, we compare with an alternative approach in which all input pixels corresponding to the same locations of the predicted high-drop pixels are reduced by 10% across all layers (all input images corresponding to all the 9 layers). For example, for testcase 7, we scale 1547 pixels in each of 9 input images at the pixels where the high-drop was predicted. As can be seen in the last column of the table (labeled ‘w/o saliency’), the number of predicted IR drop pixels actually increase on-average. Therefore saliency maps help to meaningfully reduce the number of high-drop pixels and by a significant amount, and using only a tiny portion of the PDN edges.

Figure 8 shows the high-drop pixels in the predicted IR-drop map of testcase 16 before and after optimization. The top  $K$  pixels with highest saliency on M1 are shown on the right column.

## 4 Conclusions

We presented a computer-vision based approach to predicting static IR drops in power delivery networks (PDNs) using the AtUNet model, an advanced variant of the U-Net architecture enhanced with attention mechanisms. Our findings demonstrate that AtUNet significantly surpasses previous models and 2023 ICCAD contest winner in prediction quality. The use of vector concatenation-based attention gates allows AtUNet to selectively prioritize significant areas

Table 4: Percentage reduction in the number of predicted high-drop output pixels after optimizing only the top  $K$  pixels on the input image corresponding to the highest contributor layer as identified with saliency maps.

	#Highdrop Pixels	With Saliency Maps			Without Saliency Maps	
		Layer with Highest Contribution	K=100 %Reduction	K=300 %Reduction	K=500 %Reduction	K=9×#Highdrop-Pixels %Reduction
Testcase7	1574	M1	15.00	33.30	47.25	11.07
Testcase8	2502	M1	9.69	26.70	39.774	4.52
Testcase9	550	M4	6.49	19.34	30.11	-5.51
Testcase10	364	M4	26.17	54.30	71.48	17.19
Testcase13	211	M1	8.98	21.56	34.13	1.80
Testcase14	235	M1	13.37	22.67	33.72	1.74
Testcase15	31	Via M1M4	24.47	37.23	43.62	-3.19
Testcase16	2464	M1	9.49	23.85	37.40	-6.91
Testcase19	840	M8	42.71	82.29	86.46	36.98
Testcase20	221	M1	28.47	51.60	66.55	-21.35
Average			18.48%	37.28%	49.05%	3.75%

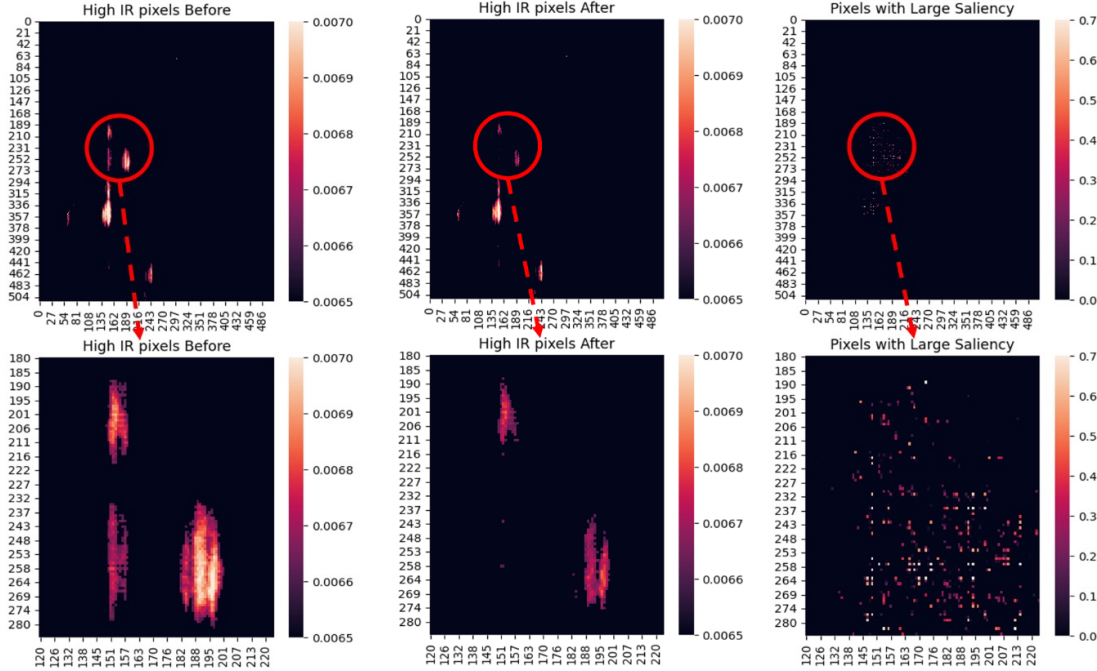


Figure 8: Predicted high-drop pixels before / after optimization (left / middle) for testcase 16. High saliency input pixels (right).

of feature maps, thus improving the accuracy and reliability of the predictions. This is particularly valuable given the sparse nature of IR drop data and the complex multi-layer structure of modern PDNs. The two-phase training process, leveraging both artificially-generated and real-world data, addresses the challenge of limited real design data and prevents overfitting. Furthermore, the use of saliency maps adds explainability to the model, making it possible to identify the significant causes of predicted high IR drops to help mitigate potential IR-drop violations.

### 5 Acknowledgements

This work is supported by a grant from National Science Foundation under Award No. 2322713.

## References

- [1] V. A. Chhabria, V. Ahuja, A. Prabhu, P. Nikhil, P. Jain, and S. S. Sapatnekar. Thermal and IR drop analysis using convolutional encoder-decoder networks. In *ASP-DAC*, pages 690–696, 2021.
- [2] J. Kozhaya, S. Nassif, and F. Najm. A multigrid-like technique for power grid analysis. In *TCAD*, volume 21, pages 1148–1160, 2002.
- [3] Y. Zhong and M. D. F. Wong. Fast algorithms for IR drop analysis in large power grid. In *ICCAD*, pages 351–357, 2005.
- [4] S. Köse and E. G. Friedman. Fast algorithms for IR voltage drop analysis exploiting locality. In *DAC*, pages 996–1001, 2011.
- [5] M. Zhao, R. V. Panda, S. S. Sapatnekar, T. Edwards, R. Chaudhry, and D. Blaauw. Hierarchical analysis of power distribution networks. In *TCAD*, volume 21, pages 159–168, 2002.
- [6] T. Chen and C. C.-P. Chen. Efficient large-scale power grid analysis based on preconditioned Krylov-subspace iterative methods. In *DAC*, pages 559–562, 2001.
- [7] C. Chou, N. Tsai, H. Yu, C. Lee, Y. Shi, and S. Chang. On the preconditioner of conjugate gradient method — a power grid simulation perspective. In *ICCAD*, pages 494–497, 2011.
- [8] S. Lin, Y. Fang, Y. Li, Y. Liu, T. Yang, S. Lin, C. Li, and E. Fang. IR drop prediction of ECO-revised circuits using machine learning. In *VTS*, pages 1–6, 2018.
- [9] S. Kundu, M. Prasad, S. Nishad, S. Nachireddy, and K. Harikrishnan. MLIR: Machine learning based IR drop prediction on ECO revised design for faster convergence. In *VLSID*, pages 68–73, 2022.
- [10] Z. Xie, H. Ren, B. Khailany, Y. Sheng, S. Santosh, J. Hu, and Y. Chen. PowerNet: Transferable dynamic IR drop estimation via maximum convolutional neural network. In *ASP-DAC*, pages 13–18, 2020.
- [11] V. A. Chhabria, K. Kunal, M. Zabihi, and S. S. Sapatnekar. BeGAN: Power grid benchmark generation using a process-portable GAN-based methodology. In *ICCAD*, pages 1–8, 2021.
- [12] CAD Contest at ICCAD. <https://drive.google.com/file/d/162C8PI1umxad3uYr06aBYgCmjeTQbvR4/view>, 2023.
- [13] K. Simonyan, A. Vedaldi, and A. Zisserman. Deep inside convolutional networks: Visualising image classification models and saliency maps. In *ICLR*, 2014.
- [14] Q. Zhang, Y. Yang, Y. Liu, Y. Wu, and S. Zhu. Unsupervised learning of neural networks to explain neural networks. *arXiv: 1805.07468*, 2018.
- [15] A. Tavanaei. Embedded encoder-decoder in convolutional networks towards explainable AI. *arXiv: 2007.06712*, 2020.
- [16] S. Seo, J. Huang, H. Yang, and Y. Liu. Interpretable convolutional neural networks with dual local and global attention for review rating prediction. In *RecSys*, pages 297–305, 2017.
- [17] O. Oktay, J. Schlemper, L.L. Folgoc, M. Lee, M. Heinrich, K. Misawa, K. Mori, S. McDonagh, B. Kainz, N. Y. Hammerla, and B. Glocker and D. Rueckert. Attention U-Net: Learning where to look for the pancreas. *arXiv: 1804.03999*, 2018.
- [18] X. Wang, R. B. Girshick, A. Gupta, and K. He. Non-local neural networks. *arXiv: 1711.07971*, 2017.
- [19] A. Krizhevsky, I. Sutskever, and G. E. Hinton. ImageNet classification with deep convolutional neural networks. In *NeurIPS*, page 1097–1105, 2012.
- [20] I. Loshchilov and F. Hutter. SGDR: Stochastic gradient descent with warm restarts. In *ICLR*, 2017.